ADVANCED FUNCTIONAL MATERIALS
www.afm-journal.de

Shadow-Thermoelectric System for Enhancing Solar Energy Harvesting and Touchless Human-Machine Interface

Chunlei Zhang, Ming Wang, Wenbo Li, Wenran Zhang, Ziling Chen, Dongming Wu, Shenghua Liu, Jing Shuai, Xuezhong He, Qian Zhang, Qijie Liang,* and Yanglong Hou**

Thermoelectric generators (TEGs) are one of the most promising means of harvesting energy from the sun. However, the TEGs require a significant temperature difference to generate electricity, making it challenging to achieve high power output from solar radiation alone. Here, shadow-effect generators (SEGs) are connected with TEGs to form a shadow-thermoelectric system (STS), which exploits the natural shadow produced by the TEG to enhance the electrical power output by solar energy conversion. With the shadow enhancement, the open-circuit voltage of the STS is significantly increased by a factor of 115 compared to that of the single TEG. Furthermore, the STSs array is successfully combined with a photoelectrochemical cell to convert the intermittent solar energy into storable hydrogen energy. In addition, the STS can be applied as a touchless self-powered sensor which provides a useful control panel for human-machine interface (HMI). After combining the STS with signal processing circuits, the STS can control a virtual vehicle on computer smartly. In conclusion, STS is a promising design for energy harvesting and touchless self-powered sensing. This research provides valuable insights for the development of efficient solar energy conversion and new possibilities for HMI.

1. Introduction

The thermoelectric generator (TEG) is an eco-friendly approach of generating electricity by collecting solar radiation and converts it, exhibiting the feature of noiselessness, long lifetime, and stable performance.[1,2] In order to optimize its efficiency, researches have adopted various approaches to maximize the electrical energy output of TEGs, including developing novel materials with high thermoelectric figure of merit,[3–5] modulation of intermolecular interactions in materials,[6] optimizing geometry of the thermoelectric legs,[7–9] and enhancing heat transfer at the hot and cold junctions.[10] However, not much engineering use has been derived from the ubiquitous shadows casting from the TEGs. The shadows cast from the TEGs even to be undesirable as they degrade the performance of the photovoltaic cells (PVCs) when the TEGs are on PVCs.[11,12] The traditional structure of TEG integrating with PVC, such as silicon-based solar cells,[13,14] dye-sensitized solar cells,[15,16] perovskite solar cells,[17–19] and so on, are with the top layer often being the PVC. This kind of structure usually are complex, expensive, and minimizing the output of TEG.[20] From 2020, the shadow-effect technique has been adopted in the field of energy conversion.[21,22] This method utilizes a shadow-effect generator (SEG) to collect energy by using the contrast between light and shadowed areas to generate electricity. The difference in the work function between illuminated and shadowed areas of the SEG creates in-plane charge transport and induces remarkable electrical output. The SEG is easy-to-fabricate, low cost, and with very good stability. Combining the TEGs with SEG is a promising approach to maximize the power output of TEGs by scavenging energy from shadows created by TEGs in a cost-convenient way.

In addition, touchless technology[23,24] is more and more important in our daily life, because of reducing the risk of spreading germs/virus by removing the need for physical touch, making things more accessible for people with disabilities, and providing an immersive experience that captures users' attention. Touchless technology in human-machine interfaces (HMI) allows users to interact with devices without physical contact.[25,26] The touchless HMI have many applications, such as automotive, smart homes, and robotics. However, the control panel with

C. Zhang, W. Zhang, D. Wu, S. Liu, J. Shuai, Q. Zhang, Y. Hou
School of Materials
Shenzhen Campus of Sun Yat-sen University
Shenzhen 518107, China
E-mail: zhangqian6@mail.sysu.edu.cn; hou@mail.sysu.edu.cn
C. Zhang, W. Li, Z. Chen, Q. Liang
Songshan Lake Materials Laboratory
Dongguan 523808, China
E-mail: liangqijie@sslab.org.cn
C. Zhang, M. Wang
School of Materials Science and Engineering
Liaoning Technical University
Liaoning 123000, China
X. He
Department of Chemical Engineering
Guangdong Technion Israel Institute of Technology
Shantou 515063, China
Y. Hou
State Key Laboratory of Optoelectronic Materials and Technologies
Sun Yat-sen University
Guangzhou 510275, China

The ORCID identification number(s) for the author(s) of this article can be found under https://doi.org/10.1002/adfm.202504693

DOI: 10.1002/adfm.202504693

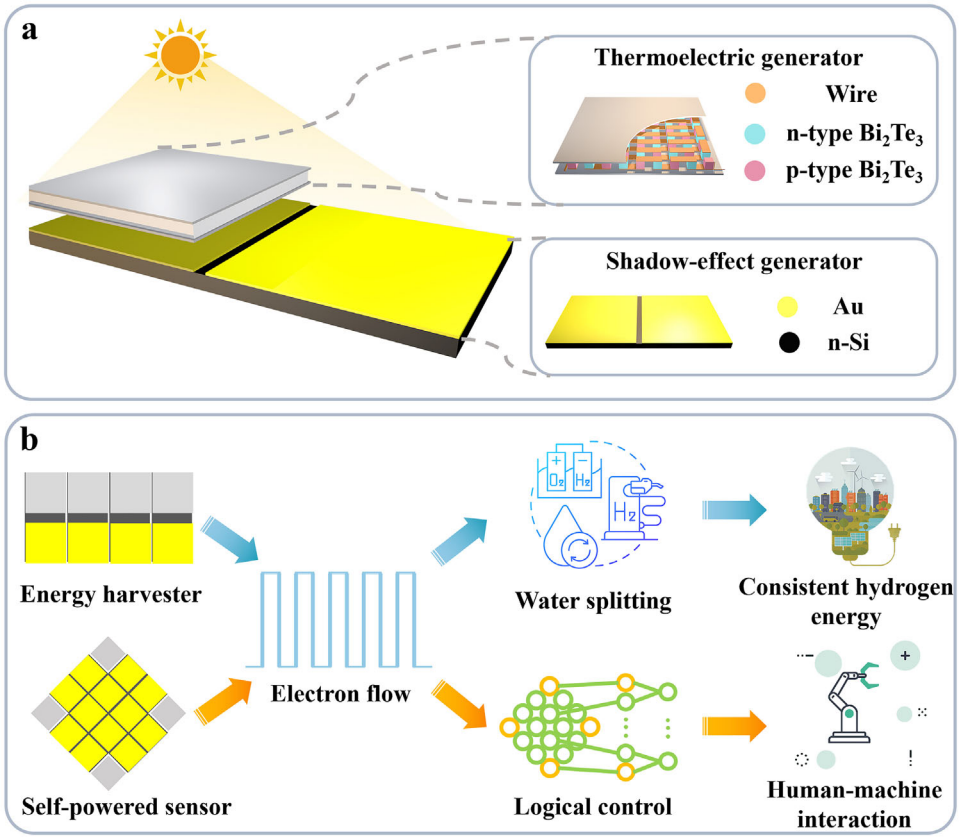

Figure 1. Design and structure of the shadow-thermoelectric system (STS). a) The structural design of the STS. b) STSs arrayed in different structures and their prospective applications which used as energy harvesters and self-powered sensors.

smart and sensitive sensor still needs to be developed. Here in this work, the TEGs are combining with the SEGs to form a shadow-thermoelectric system (STS) for enhancing solar energy harvesting. With this combination, the solar energy is converted into electricity not only through the Seebeck effect[27] by TEG, but also shadow-effect by SEG simultaneously. To demonstrate potential of the STS in applications, the photoelectrochemical cell (PEC) is further integrating with STS to convert intermittent solar energy into storable hydrogen energy. Meanwhile, the STS has the capability of utilizing as self-powered sensor in touchless technology by detecting temperature and shadows signal variations uncontacted. In the future, the STS has the potential to play an important role in the fields of renewable energy, internet of things (IOT)and smart city control systems, contributing to the development of green and smart technologies.

2. Results

The schematic diagram of the STS is presented in **Figure** 1a. The structure of the STS comprises two principal components: i) SEG comprising a 15 nm-thick Au film deposited on n-type Si using thermal evaporation. ii) TEG comprising multiple pairs of p-type Bi_2Te_3 and n-type Bi_2Te_3 compounds, which are connected in series by wires. The micro-morphology of the disassembled and encapsulated TEG was characterized by scanning electron microscopy (SEM), as illustrated in Figure S1 (Supporting Information). The structure is composed of dense platelets with some fine particles. To improve the output voltage and reduce crosstalk between TEG and SEG parts, the TEG is encased in a ceramic package with high thermal conductivity. As shown in Figure 1b, the STSs could be arrayed in different structures and then used as energy harvester and self-powered sensor. When the STSs array functionalizing as energy harvesters, the TEGs on the top casts the shadow on SEGs, creating spatially resolved light-shadow contrast. This contrast drives the work function gradient of SEG, which is essential for generating the SEG's open-circuit voltage (V_{oc}). The generated electron flow is further used to split water to convert the intermittent solar energy to consistent hydrogen energy. Second, when the STSs array functionalizing as self-powered sensor, they can be used to recognize hand gestures by detecting temperature and shadows signal variations touchless. After combining the STSs array with signal processing circuits, the STS can enable touchless HMI. To achieve a higher output power in the same illuminated area, two TEGs are positioned at the bottom of the SEG.

To clarify how the additive effect allows the STS to harvest energy from both shadow-effect and thermal gradients, a model that a TEG located at the top of the SEG is shown in **Figure** 2a. The TEG is connected in series with the SEG and creates shadows and illuminated areas on the SEG. The work function gradient is formed on the Au film of SEG due to the bright and shadowed areas caused by illumination, which produces an

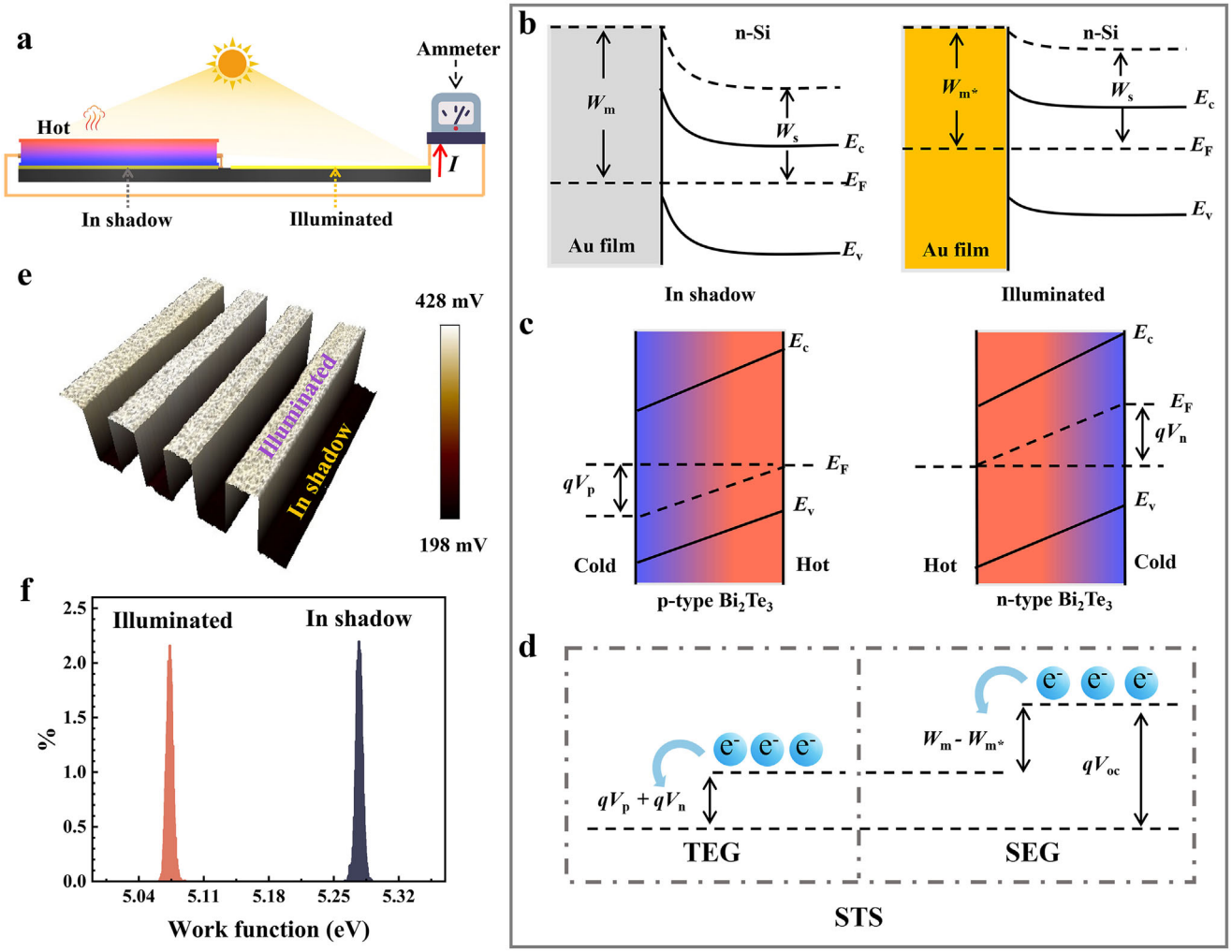

Figure 2. Schematic illustration and physical mechanism of the shadow-thermoelectric system (STS) operation. a) The structure of the STS which intergraded thermoelectric generators (TEG, red and blue one on the top) with shadow-effect generator (SEG, black one beneath the TEG) used as an energy harvester. b) Mechanism diagram of SEG, c) TEG, d) STS. e) Surface potential map and f) work function shifts of a 15 nm Au film under dark and illuminated conditions for both in shadow and under illumination.

shadow-electromotive force. The energy band diagrams in the shadow and in illumination conditions are shown in Figure 2b. The shadow-electromotive force can be calculated using the following Equation (1):

$$V_{oc\ SEG} = \left(W_m - W_{m*}\right)/q \tag{1}$$

where $V_{oc\ SEG}$ is the V_{oc} generated by the SEG, W_m is the work function of the Au film in the shadow area, W_{m*} is the work function of the Au film in the illuminated area, and q is the electron charge.

The concentration of carriers in the n-type and p-type materials of the TEG increases exponentially as the temperature rises, in the case of uniform doping and unsaturated materials. The diffusion of carriers from the hot side to the cold side results in a shift of the Fermi level toward the intrinsic Fermi level. An electric filed is formed within the semiconductor interior once the drift and diffusion of carries have reached equilibrium, resulting in an thermal-electromotive force between the two terminals of the TEG. This thermal-electromotive force refers to the thermoelectric V_{oc} induced by the temperature gradient. The thermal-electromotive force can be calculated by the Equation (2):

$$V_{oc\ TEG} = V_p + V_n \tag{2}$$

The $V_{oc\ TEG}$ is the V_{oc} produced by the TEG, V_p and V_n are the sum of the thermoelectric potentials generated by all of the p-type Bi_2Te_3 and n-type Bi_2Te_3 in the TEG, respectively. The relative energy band diagram of the TEG is shown in Figure 2c. The V_{oc} of the STS ($V_{oc\ STS}$) is defined by the Equation (3), and its energy band diagram is shown in Figure 2d.

$$V_{oc\ STS} = V_{oc\ SEG} + V_{oc\ TEG} \tag{3}$$

Figure 2e shows the surface potential results of the Au film, which is characterized under alternating illumination and

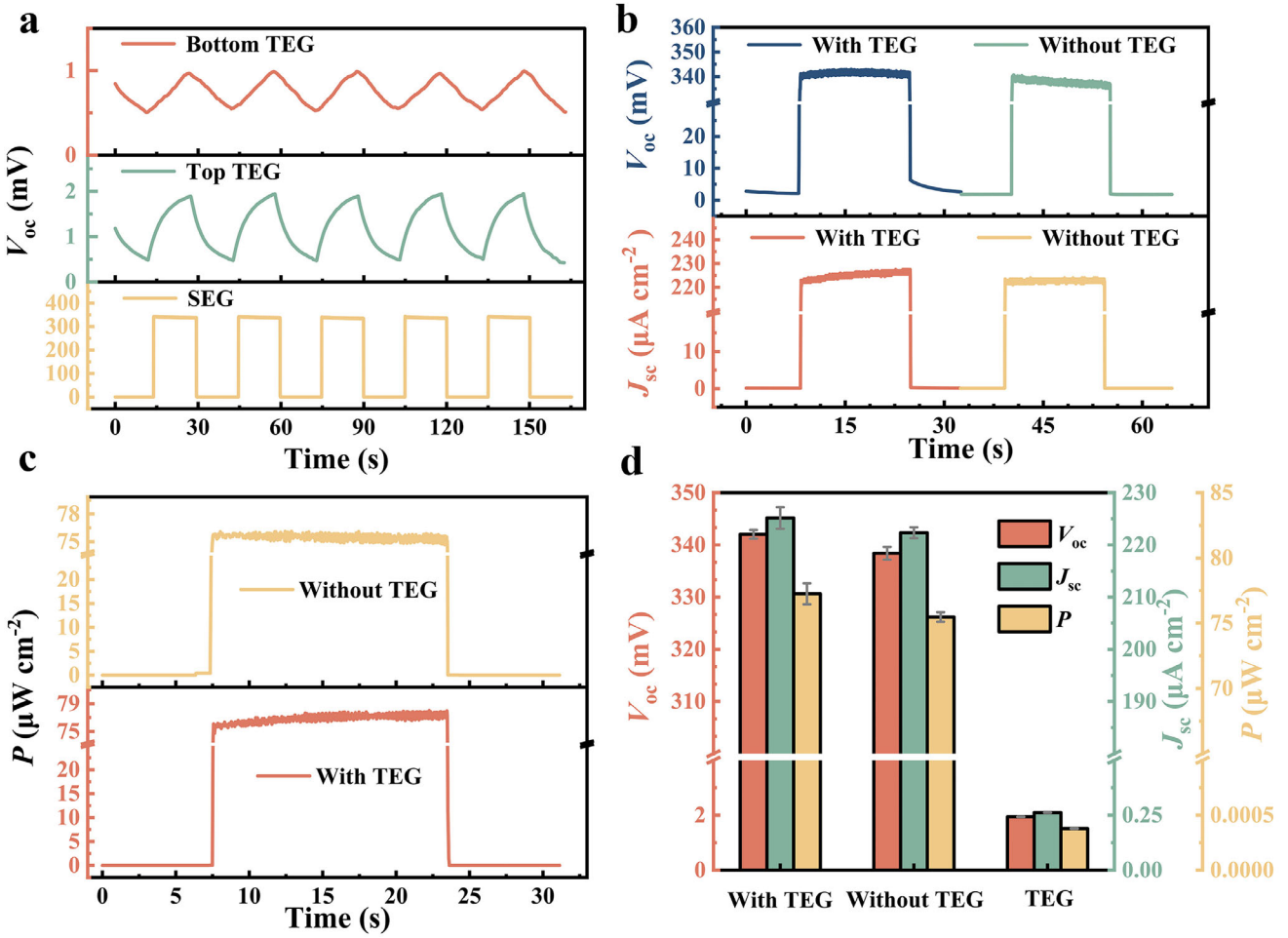

Figure 3. Performance characteristics of the shadow-thermoelectric system (STS). a) Open-circuit voltage (V_{oc}) of thermoelectric generator (TEG) and shadow-effect generator (SEG). b) V_{oc} and short-circuit current density (J_{sc}) of the shadow-thermoelectric system (STS) with and without TEGs. c) Power density (P) comparison of the STS with and without TEGs. d) Comparison of the V_{oc}, J_{sc}, and P of STS with and without TEGs, TEGs.

darkness at a low light intensity of ≈0.01 sun by kelvin probe force microscopy. The results indicate that the surface potential under illumination is higher than that of in the dark. The calculated difference in work function between the illuminated and dark conditions is 0.2 eV, as shown in Figure 2f. The related discussion of the work function on the surface of Au/n-Si is presented in Note S1 (Supporting Information).

The V_{oc} and short-circuit current density (J_{sc}) of the TEG were measured in dark and 1000 W m^{-2} illuminated pulses in the conditions of room temperature and without any auxiliary cooling devices. The detailed surface temperature changes of TEG hot side can be found in Figure S2 (Supporting Information). As shown in **Figures** 3a and S3 (Supporting Information), the V_{oc} and J_{sc} of the TEG gradually increased with the increase of light time, and the V_{oc} at the bottom position compared to the maximum values at the top position were 1.21 and 1.98 mV, respectively, which was a 77% increase compared to the bottom. Much more enhancements in the V_{oc} and J_{sc} are observed in TEG on the top because of the more increases in temperature variations than bottom TEGs.

The optimal SEG performance was determined with 15 nm Au by systematically investigating the performance influence of Au film thickness, as shown in Figure S4 (Supporting Information). At the same time, the STS exhibits higher V_{oc} (344 mV) and J_{sc} (225 μA cm^{-2}) under the condition of half-area shadow by the TEG with 1000 W m^{-2} illumination. Figure 3b shows the V_{oc} and J_{sc} of the STS differ from those of with and without TEGs under dark and illumination pulse conditions. Further details regarding the J_{sc} data of SEG, TEG and STS can be found in Figure S3 (Supporting Information). The TEG generates electricity vial the Seebeck effect from temperature gradients induced by solar heating. While its standalone output voltage is small, it additively contributes to the total output of STS. For the STS without TEGs, there is a phenomenon in single SEG that the V_{oc} under high temperature exhibits a decreasing trend over time. This phenomenon can be attributed to the recombination of electrons and holes as the operating temperature of the n-Si increases, which leads to a decrease in the V_{oc}. Meanwhile, the V_{oc} of STS exhibit a stable trend under 1000 W m^{-2} continuously illuminated. This is because of the compensation from the V_{oc} of TEGs. As the

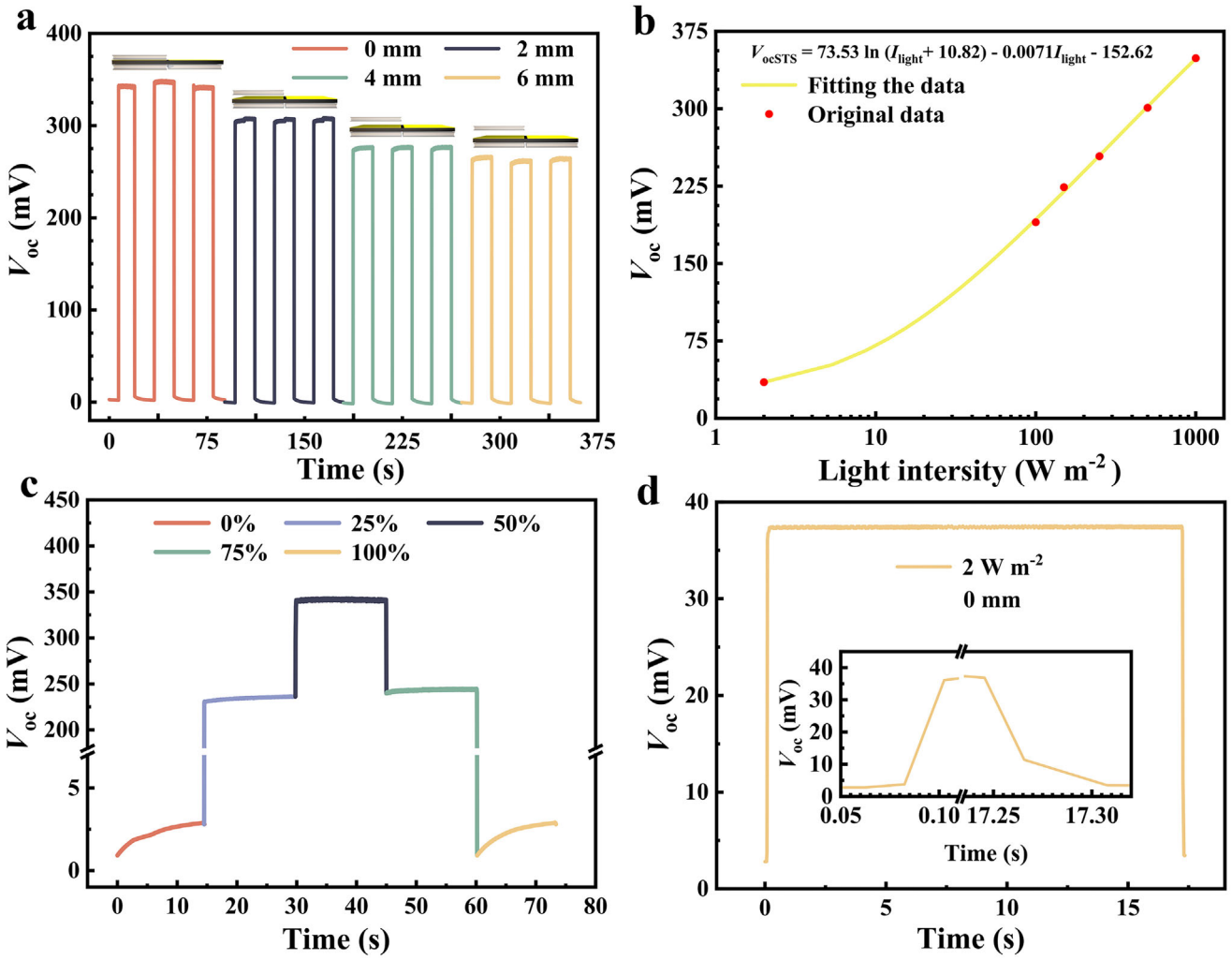

Figure 4. Factors that influence the performances of shadow-thermoelectric system (STS). a) The influence of vertical distance between the thermoelectric generator (TEG) and the shadow-effect generator (SEG) on the V_{oc} of the STS. b) Comparison of the STS under different light intensities and fitted curve. c) The impact of obstructing the TEG at distinct positions on the STS. d) The response time of the STS under 2 W m^{-2} light intensity illumination, insert is the details of the response curve when the light on and off.

duration of illumination increased, the temperature difference between the hot and cold sides of the TEGs gradually increased, resulting in a corresponding increase in the V_{oc} of the TEGs. Meanwhile, as the duration of illumination increased, the J_{sc} exhibited a slight increase. Figure 3c illustrates that the power density (P) of the STS without TEGs integration exhibited a decreasing trend as the increase in irradiation time, whereas the STS shows a gradual growth since the presence of the TEGs. The power density of the STS was calculated by the Equation (4).

$$P = \frac{V_{oc}J_{sc}}{A} \tag{4}$$

where A is the area of the STS under illumination. To assess the overall performance of the STS, a comparative analysis was conducted on the power, V_{oc}, and J_{sc} of the STS with and without TEGs. As shown in Figure 3d, the P of the STS surpasses ≈ 2.2% than the sum of that produced by the independent TEGs and the SEG. With the enhancement of SEG, the V_{oc} of the STS is significantly increased by a factor of 115 compared to that of the TEGs. These results demonstrate the output of STS is increased by the integration of SEG and TEGs.

In order to ascertain the potential applications of the SEG in different scenarios, a systematic evaluation and analysis of the comprehensive performance of STS under different conditions is conducted. This involved a detailed analysis of factors such as the spacing structure of STS, illumination intensity, the area of the shadowed region on SEG casting by TEG, and the response time of the STS. **Figure** 4a demonstrates the influence of the spacing structure such as vertical distance between the TEG which is on the top and the SEG. As the distance between the two components increases, the intensity of the shadow cast by the TEG onto the SEG gradually diminishes, resulting in a decline in the V_{oc} of the SEG. The reduction in shadow intensity has a significant impact on the diminished light contrast, which in turn has a negative effect on the V_{oc} of the STS. It is significant to note that

the STS continues to demonstrate a relatively remarkable V_{oc} at a greater distance. This directly illustrates the role of spatial structure in regulating the shadow distribution within the SEG, and thus indirectly determines STS overall performance characteristics, which lays an experimental foundation for touchless sensing applications. The points in Figure 4b illustrates the performance of the STS under different illumination intensities. The results demonstrate an upward trend in the V_{oc} of the STS as the illumination intensity increases in sequence from 2, 100, 150, 250, 500, to 1000 W m^{-2}. The dataset was conducted with fitting analysis to find the quantitative relationship between the V_{oc} of the STS and light intensity. The fitted curve in Figure 4b obtained by a hybrid fitting model:

$$V_{oc\ STS} = A\ln(I_{light} + B) + CI_{light} + D \quad (5)$$

where I_{light} is the light intensity, Aln (I_{light} + B) captures the SEG's logarithmic dependence CI_{light}represents the TEG's linear response to temperature gradients, D accounts for baseline offsets. From the fitting modulation and the raw data from Figure 4b, the STS exited V_{oc} dependence on light intensity with a relationship of A = 73.53, B = 10.82, C = -0.007, D = -152.62. The fitted curve provides a quantitative basis for analyzing the relationship between the SEG and TEG, the higher the light intensity, the more obvious the V_{oc} enhancement. The results of J_{sc} are also tested and shown in Figure S5 (Supporting Information). As shown in Figure 4c, the influence of the shadow area generated by the TEG was examined by placing the TEG at different locations. When the TEG and SEG are arranged parallel and adjacent to each other, there is no shadow on the SEG under illumination, which is the ratio of shadowed area of 0% condition. In the 0% condition, the SEG in the STS is unable to generate electricity directly and the contribution of STS V_{oc} is all form TEGs. A black paper is used to cooperate the TEG on the top to make a shadowed area ratio of 100%. In the 100% condition, the TEG can utilize the residual heat during the subsequent darkness period due to the Seebeck effect, which results in a small V_{oc}. This phenomenon serves to highlight the significant advantages of the STS in energy recovery and sustained power generation, particularly in environments where continuous light illumination is not feasible. It illustrates the capacity to provide power for a range of compact electronic devices. The V_{oc} of the SEG varies at 25%, 75%, and half-shading (50%) conditions while the optimal performance is achieved in the half-shading condition with a peak V_{oc} approaching 344 mV. Figure S6 (Supporting Information) shows the related results of J_{sc}. Figure 4d illustrates the response time of the STS under low light intensity (2 W m^{-2}). Even under low-light intensity environments, the STS demonstrates a commendable transient response capability with a response time of ≈ 20 ms, indicating that the series connection of its components has no significant impact on its responsiveness. The STS not only exhibits outstanding energy harvesting capabilities, but also possesses the potential to function as a self-powered sensor. The performance of the STS is influenced by the impact and modulation of various conditions, demonstrating its distinctive sensitivity and adaptability. It is capable of detecting temperature and shadows signal variations in dynamic natural environments.

In order to further investigate the potential of the STS in harvesting solar energy, a combination of four STSs array with a PEC was created. The STSs array, combined with the PEC cell, converts intermittent solar energy into storable hydrogen. The contribution of TEG ensures continuous operation during low-light periods such as cloudy but with large temperature difference day. The circuit diagram of the combination is depicted in **Figure 5a**. The photoanode material of the PEC is chosen to be $BiVO_4$ (BVO), which has been modified by depositing with $FeCoO_x$ (FCO). The micro-morphology was characterized by SEMscanning electron microscopy (as shown in Figure S7 (Supporting Information). As illustrated in Figure 5b, the results of linear sweep voltammetry (LSV) shows that the current response of BVO-FCO is much better than pure BVO. The introduction of FCO on the BVO results in a reduction of the holes and electrons recombination, thereby enhancing the overall current density. As shown in Figure 5c, the J_{sc} of the BVO-FCO photoanode is significantly greater than that of the pure BVO, with an enhancement exceeding 50% under 1 sun illumination. The electrochemical impedance spectroscopy shown in Figure S8 (Supporting Information) also illustrates the performance of BVO-FCO is better than pure BVO, which is consistent with the LSV results. Above all, the BVO-FCO is an optimal choice for the photoanode materials of PEC, which can be combined with STSs array to form a more efficient energy converter. As shown in Figure 5d, the peak current density of the STSs array combined with BVO-FCO PEC cell was measured as 1.38 mA cm^{-2} under light intensity of 1000 W m^{-2}. The current density data are the same in the 8 illuminated and dark cycles, indicating the combination of STSs array and BVO-FCO PEC cell is stable. The long-term illumination test results in Figure S9 (Supporting Information) demonstrate the stability of the combination. To investigate the contributions of the TEGs to splitting water stably, the current density of the STSs water splitting system without TEGs were calculated by theoretical analysis (Figure S10, Supporting Information). The combination of the STSs array and PEC for water splitting demonstrates significant potential for stable and renewable applications. To explore the optimal external impedance of the STSs array, resistors were connected with the four STSs array to systematically study the optimum matching impedance. As shown in Figure 5e, the output power of the STSs array reaches a peak value of 15.89 μW cm^{-2} when connected to a resistor of 2.7 kΩ, corresponding to a J_{sc} of 27.13 μA cm^{-2}.

The STS is capable of producing electrical signals in response to temperature and shadows signal variations without physical contact, which makes it a strong candidate to touchless self-powered sensor. As shown in **Figure 6a**, four TEGs are set onto the 4×4 SEG array and the formed STS arrays have 20 channels to connect with signal processing circuits (Mega 2560). The relative positions of the SEG, TEG, and STS were kept fixed throughout the test. At the same time, the room temperature was precisely controlled at 26 °C to provide stable temperature conditions for the experiment. To demonstrate the function of the STS arrays, the channels from 1 to 8 (C1, C2, C3, C4, C5, C6, C7, C8 as shown in Figure 6a) were used in this work. Then the signals caused by shadow-effect from SEG and Seebeck effect from TEG can realize different controlment, such as direction and speed control in a virtual vehicle by HMI. Considering that current HMI control typically entails high determinism, clear causal relationships, and stable environmental conditions, it is appropriate to employ logical control strategies to realize sen-

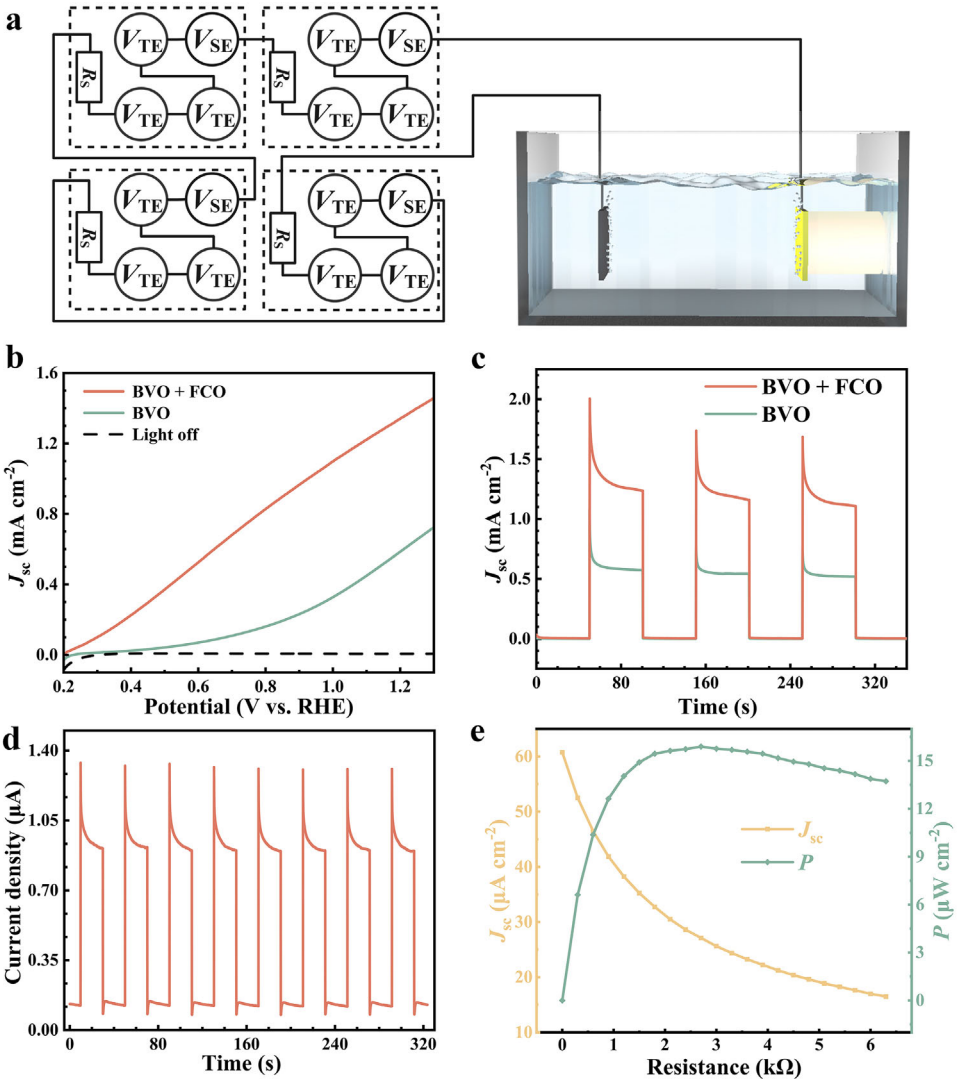

Figure 5. The performance of shadow-thermoelectric systems (STSs) array combined with photoelectrochemical (PEC) cells. a) The circuit diagram of the combination between STSs array and PEC cell. b) The linear sweep voltammetry (LSV) curves of $BiVO_4$ (BVO) and $FeCoO_x$ deposited BVO (BVO-FCO) electrodes. c) Chronoamperometric measurements of the BVO and BVO-FCO photoanodes in 0.5 M potassium phosphate buffer (pH 7). d) The current density of the STSs array combined with PEC cell under 1000 W m^{-2} illumination and dark cycles (BVO-FCO photoanode in 0.5 M potassium phosphate buffer (pH 7)). e) The J_{sc} and power density of the STSs array under different external loads.

sory operations. The STSs arrayed self-powered sensor, which is able of detecting shadow and heat without physical contact, can be employed to identify the gesture from human hand. This enables the orientation of an object to be controlled or forward commands to be executed, thereby facilitating the realization of HMI operations. In conditions of indoor light (2 W m^{-2}), the STSs arrayed self-powered sensor is able to differentiate between shadows created by different gestures, thereby enabling the orientation control of the HMI. The signal is then transmitted to an HMI simulation program via a microcontroller, where it is utilized to achieve directional control based on the signals produced by the distinct units, as illustrated in Figure 6b. This technology is particularly well-suited to non-contact vehicle control systems, thereby enhancing convenience. Upon the finger close to the TEG of the STS-arrayed self-powered sensor, the TEG has the ability to detect heat change. The utilization of this thermal sensing property allows for the design of a control system for the vehicle's driving speed as shown in Figure 6c. This STS-arrayed self-powered sensor serves to illustrate the potential for touchless HMI operations by controlling the constant speed movement of objects as an example. As shown in the Supplementary Movie S1, under indoor light conditions, the voltage generated by the position of the shadow cast by the finger can be used to control the direction of motion of the vehicle, which is equivalent to a steering wheel. When the TEG detects the temperature of the finger is closing, the voltage signal generated by TEG is used to control the forward movement of the vehicle, similar to controlling the gas pedal. In HMI applications, the thermal response of TEG complements the shadow detection of SEG, enabling complex commands (e.g., speed control via

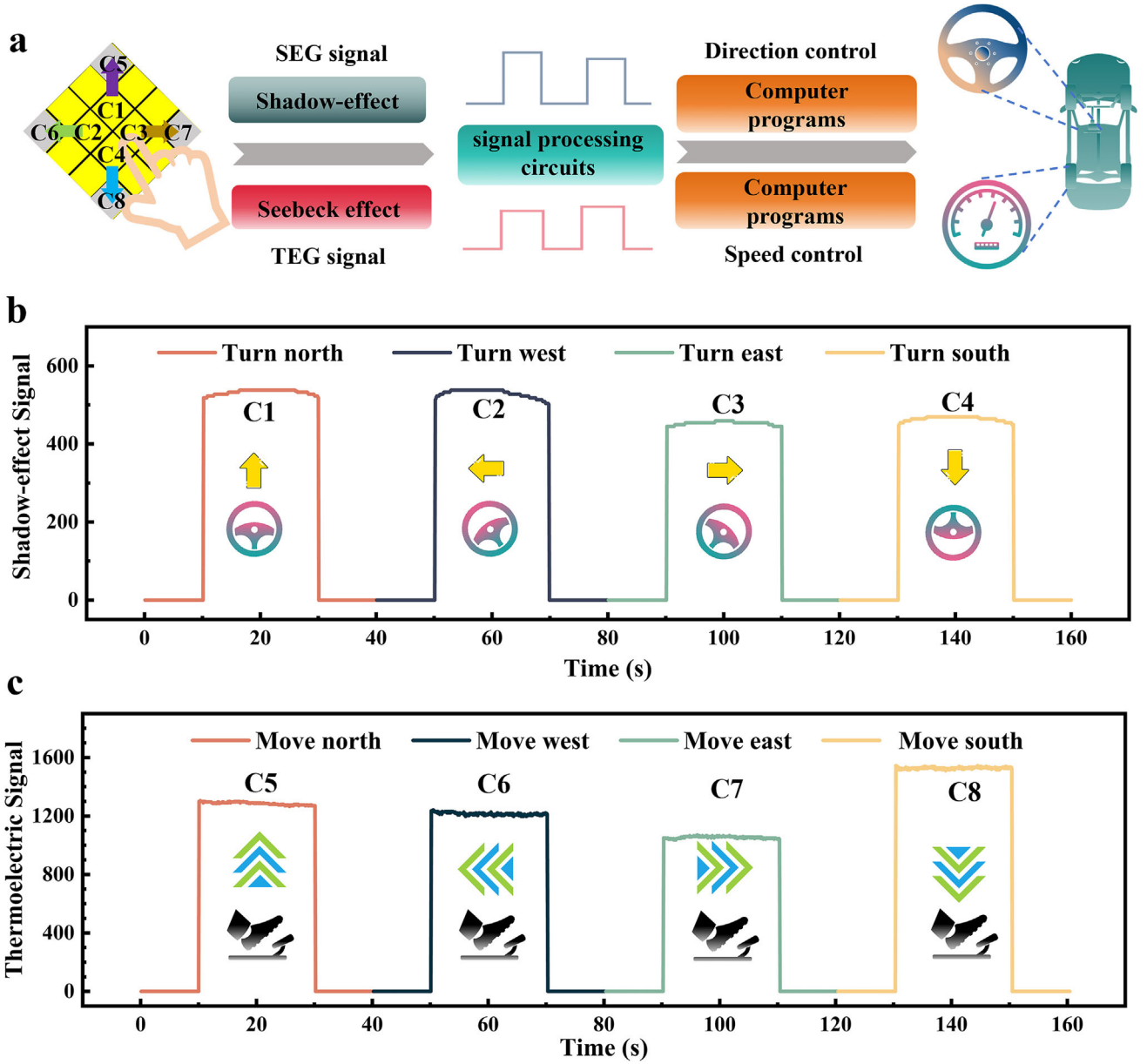

Figure 6. Shadow-thermoelectric systems (STS)-arrayed self-powered sensor for touchless human-machine interaction (HMI). a) Schematic diagram of HMI with STS-arrayed self-powered sensor. b) The response signals of different shadow positions are used to control the direction of the vehicle. c) The manipulation of vehicle speed through foreclose to thermoelectric generator (TEG).

heat and direction via shadows). In conclusion, the STS-arrayed self-powered sensor represents a viable solution for the control panel of touchless HMI.

3. Conclusion

By integrating TEG with SEG, the STS not only enhances the absorption efficiency of the infrared portion of the solar spectrum, but also adeptly harnesses the shadow produced by the TEG to generate electricity. This process is contingent upon the variation in the work function of Au films under different illumination-shadow conditions. Moreover, the STS effectively addresses the issue of intermittent power supply by pairing it with a photoelectrochemical device, thereby facilitating energy storage and subsequent utilization, and ensuring a more stable and reliable power supply. Additionally, the STS possesses self-sensing capabilities that can detect temperature fluctuations, changes in shadow, and gesture commands with sensitivity, offering novel avenues for human-machine interaction. Looking ahead, the STS is anticipated to become a crucial component of the renewable energy sector and play a pivotal role in intelligent perception and human-machine interaction technology, providing robust technical support for the construction of a sustainable energy system.

4. Experimental Section

Manufacturing of the SEG: The SEG was fabricated using n-type silicon wafers with a thickness of 530 µm and a resistivity of 0.001 Ω cm^{-1}. They were cut to the specified size and then ultrasonically cleaned with isopropanol, ethanol, and deionized water. After cleaning, the wafers were dried using nitrogen gas. Subsequently, Au was deposited onto the silicon wafer using thermal evaporation, with a deposition thickness of 15 nm. The deposition rate is 0.5 Å s^{-1}. Thermal evaporation starts when the vacuum degree is 1.0×10^{-4} Pa.

Manufacturing of Photoanode: Electrodeposition of BiOI Templates: BiOI films were first electrode-posited to serve as the precursor films to form BVO electrodes. Briefly, an FTO substrate (14 ohm per square, NOZO, China) was used as the work electrode (WE), and a platinum foil was used as the counter electrode (CE). The reference electrode (RE) was an Ag/AgCl electrode in 1 M KCl solution. The plating solution was prepared by dissolving 30 mm $Bi(NO_3)_3$ (Aladdin, 99%) in 400 mm KI (Aladdin, 99%) aqueous solution (50 mL). 100 mm p-benzoquinone (Aladdin, 99%) in absolute ethanol was then added to the solution. The mixture was vigorously stirred for a few minutes. The cathodic depositions were carried out potential statically at −0.15 V versus Ag/AgCl at room temperature. Conversion of BiOI Films to BVO Films: The 0.1 mL dimethyl sulfoxide solution (Aladdin, 99%) containing 200 mm vanadyl acetylacetonate (Aladdin, 99%) was dropped onto the BiOI template. The sample was then annealed in air at 450 °C for 2 h. After the annealing, excessive V_2O_5 present in the BVO was removed by soaking in a 1 M NaOH (Aladdin, 99%) solution. $FeCoO_x$ Cocatalyst Deposition on the BVO Film: The $FeCoO_x$ cocata-lysts were deposited using a two-step electrodeposition. First, a FeOOH layer was deposited from a 0.1 M $FeSO_4 \cdot 7H_2O$ (Aladdin, 99%) solution at 0.25 V versus Ag/AgCl for 5 min. Then, CoO_x was deposited from a 25×10^{-3} M $(CH_3COO)_2Co \cdot 4H_2O$ (Aladdin, 99%) solution at 0.25 V versus Ag/AgCl for 80 s, respectively. Finally, the films were annealed at 500 °C for 2 h in air, denoted as BFC.

Architecture of the STS: Electrodeposition of BiOI Templates: BiOI films were first electrode-posited to serve as The SEG unit used for performance characterization has dimensions of 2 cm × 1 cm for the SEG and 1 cm × 1 cm for the TEG. The TEG is a commercially purchased, pre-encapsulated unit with its composition being bismuth telluride. The SEG used for electrolyzing water is an array formed by four SEG devices connected in series. The SEG device used for sensing and control is constructed from a 4 cm × 4 cm SEG and four 1 cm × 1 cm TEG devices. The SEG is placed on a substrate printed with EBS material, with the four TEG devices placed beside the SEG on its four sides.

Experimental Measurement and Characterization: In the performance characterization section, both V_{oc} and J_{sc} measurements were completed using the Keithley K2400. The illumination device utilized a desk lamp with an intensity of 2 W m^{-2} and a xenon lamp to simulate sunlight. The illumination intensity was measured using a solar power meter (model IM-750). To ensure the accuracy and reliability of the experimental data, the light intensity of the light source was measured three times with solar power meter before each test. Temperature measurements were conducted using the EX6000. After turning on the light source, each device was measured at least three times, and the average of the measured data was taken. During the test, the SEG device remained below the light source. The Kelvin probe force microscopy, electrochemical workstation. At an illumination intensity of 2 W m^{-2}, the simulated V_{oc} signal generated by the SEG was collected and processed by the Arduino Mega 2560. The morphologies of the films photoanode were characterized by SEM (JSM-IT500, JEOL). The relative positions of the SEG, TEG, and STS were kept fixed throughout the test, and the light source instrument was always placed at the initial set position to ensure the spatial stability of the experimental environment. At the same time, the room temperature was precisely controlled at 26 °C to provide stable temperature conditions for the experiment. It is worth noting that in order to ensure the accuracy and reliability of the experimental data, the light intensity of the light source was measured three times with professional light intensity measurement equipment before each test. If the deviation between the three measurements exceeds the preset range, the light source will be debugged or recalibrated until the light intensity data is stable and meets the experimental requirements, and then the test will be formally started in order to minimize the impact of fluctuations in light intensity of the light source on the results of the experiment.

The STS as a Self-Powered Sensor in the Development of HMI: The HMI system was developed using the Python programming language. It relies on the versus-code compiler to perform serial communication by calling the pygame and serial modules in Python. The processed data characteristics transmitted through serial communication are used to complete human-machine interaction operations. The Arduino module is used for program development on the Arduino development board. At the same time, the csv-module can be called to complete data saving.

Supporting Information

Supporting Information is available from the Wiley Online Library or from the author.

Acknowledgements

C.Z. and M.W. contributed equally to this work. This work was financially supported by the National Key R&D Program of China (Grants No. 2024YFB3817400, 2024YFA1211400), the Guangdong Basic and Applied Basic Research Foundation (Grants No. 2023B1515120041, 2023A1515012072, 2022A1515110619), the National Natural Science Foundation of China (Grant No. 52202183), the Shenzhen Science and Technology Program (Grant No. 202206193000001), the Open Project Fund from Guangdong Provincial Key Laboratory of Materials and Technology for Energy Conversion (MATEC2023KF003), State Key Laboratory of Optoelectronic Materials and Technologies (Sun Yat-sen University, Grant No. OEMT-2024-ZXT-04), Open Research Fund of Songshan Lake Materials Laboratory (2023SLABFK06).

Conflict of Interest

The authors declare no conflict of interest.

Author Contributions

Q.Z., M.W., Q.L., and Y.H. performed conceptualization. C.Z., W.L., and W.Z. performed methodology. S.L., C.Z., D.W., and M.W. performed investigation. C.Z. and M.W. performed visualization. Q.Z., M.W., and Q.L. performed supervision. Q.Z., M.W., Q.L., Z.C., and C.Z. wrote-original draft. Q.Z., Q.L., J.S., X.H., and M.W. wrote-review and edited.

Data Availability Statement

The data that support the findings of this study are available from the corresponding author upon reasonable request.

Keywords

human-machine interface, self-powered sensor, shadow-effect, solar water splitting, thermoelectric

Received: February 20, 2025
Revised: April 1, 2025
Published online:

[1] L. Miao, S. Zhu, C. Liu, J. Gao, Z. Zhang, Y. Peng, J.-L. Chen, Y. Gao, J. Liang, T. Mori, *Nat. Commun.* **2024**, *15*, 8516.

[2] M. Feng, S. Lv, J. Deng, Y. Guo, Y. Wu, G. Shi, M. Zhang, *Renew. Sustain. Energy Rev.* **2023**, *187*, 113723.
[3] J. Li, W. Liu, W. Xu, H. Zhuang, Z. Han, F. Jiang, P. Zhang, H. Hu, H. Gao, Y. Jiang, B. Cai, J. Pei, B. Su, Q. Li, K. Hayashi, H. Li, Y. Miyazaki, X. Cao, Q. Zheng, J. Li, *Adv. Mater.* **2023**, *35*, 2209119.
[4] Y. Jiang, J. Dong, H.-L. Zhuang, J. Yu, B. Su, H. Li, J. Pei, F.-H. Sun, M. Zhou, H. Hu, J.-W. Li, Z. Han, B.-P. Zhang, T. Mori, J.-F. Li, *Nat. Commun.* **2022**, *13*, 6087.
[5] J. Yuan, T. Deng, P. Qiu, Z. Li, Z. Zhou, C. Ming, Y. Xiong, C. Ma, X. Shi, *Adv. Funct. Mater.* **2024**, *34*, 2402546.
[6] C. Fang, R. Almughathawi, Q. Wu, W. Cao, H. Chen, S. Hou, Y. Gu, H. Zhang, Y. Zhao, J. Zheng, G. Li, J. Shi, J. Liu, B.-W. Mao, Z. Liu, C. J. Lambert, W. Hong, *Nat. Sci. Open* **2023**, *2*, 20220039.
[7] X. Li, Z. Zhu, K. Behnia, *Adv. Mater.* **2021**, *33*, 2100751.
[8] J. S. Sun, *Nat. Energy* **2024**, *9*, 1060.
[9] D. Zhang, N. Ngoh Yen Qi, S. Faye Duran Solco, X. Li, A. Suwardi, *ACS Energy Lett.* **2024**, *9*, 2240.
[10] M. M. Bernal, A. Di Pierro, C. Novara, F. Giorgis, B. Mortazavi, G. Saracco, A. Fina, *Adv. Funct. Mater.* **2018**, *28*, 1706954.
[11] J. Appelbaum, J. Bany, *Sol. Energy* **1979**, *23*, 497.
[12] D. König, G. Ebest, *Sol. Energy Mater. Sol. Cells* **2003**, *75*, 381.
[13] J. Darkwa, J. Calautit, D. Du, G. Kokogianakis, *Appl. Energy* **2019**, *248*, 688.
[14] A. Kane, V. Verma, B. Singh, *Renew. Sustain. Energy Rev.* **2017**, *75*, 1295.
[15] S. Su, T. Liu, Y. Wang, X. Chen, J. Wang, J. Chen, *Appl. Energy* **2014**, *120*, 16.
[16] T. Chen, G. H. Guai, C. Gong, W. Hu, J. Zhu, H. Yang, Q. Yan, C. M. Li, *Energy Environ. Sci.* **2012**, *5*, 6294.
[17] Z. Liu, B. Sun, Y. Zhong, X. Liu, J. Han, T. Shi, Z. Tang, G. Liao, *Nano Energy* **2017**, *38*, 457.
[18] L. Xu, Y. Xiong, A. Mei, Y. Hu, Y. Rong, Y. Zhou, B. Hu, H. Han, *Adv. Energy Mater.* **2018**, *8*, 1702937.
[19] Q. Li, Y. Zhang, G. Zhang, Y. Wang, H. Pang, *Nat. Sci. Open* **2023**, *2*, 20220065.
[20] A. S. Mundada, K. K. Shah, J. M. Pearce, *Renew. Sustain. Energy Rev.* **2016**, *57*, 692.
[21] Q. Zhang, Q. Liang, D. K. Nandakumar, S. K. Ravi, H. Qu, L. Suresh, X. Zhang, Y. Zhang, L. Yang, A. T. S. Wee, S. C. Tan, *Energy Environ. Sci.* **2020**, *13*, 2404.
[22] Q. Zhang, Q. Liang, D. K. Nandakumar, H. Qu, Q. Shi, F. I. Alzakia, D. J. J. Tay, L. Yang, X. Zhang, L. Suresh, C. Lee, A. T. S. Wee, S. C. Tan, *Nat. Commun.* **2021**, *12*, 616.
[23] J. Wang, W. Lin, Z. Chen, V. O. Nikolaeva, L. O. Alimi, N. M. Khashab, *Nat. Commun.* **2024**, *15*, 1575.
[24] H. L. Wang, Y. Wang, *ACS Nano* **2023**, *17*, 20723.
[25] H. Zhou, W. Huang, Z. Xiao, S. Zhang, W. Li, J. Hu, T. Feng, J. Wu, P. Zhu, Y. Mao, *Adv. Funct. Mater.* **2022**, *32*, 2208271.
[26] P. Makushko, E. S. Oliveros Mata, G. S. Cañón Bermúdez, M. Hassan, S. Laureti, C. Rinaldi, F. Fagiani, G. Barucca, N. Schmidt, Y. Zabila, T. Kosub, R. Illing, O. Volkov, I. Vladymyrskyi, J. Fassbender, M. Albrecht, G. Varvaro, D. Makarov, *Adv. Funct. Mater.* **2021**, *31*, 2101089.
[27] J. He, T. M. Tritt, *Science* **2017**, *357*, aak9997.

